SUPPLEMENTARY METHODS, DATA, AND FIGURES

Whole-Slide High-Resolution Image Acquisition

Images were acquired using the Olympus FV3000 laser scanning confocal microscope, with motorized stages and 2x PlanApo N and 40x UPlanSApo objective microscope lenses. The system used all diode lasers with a galvanometer scanner and multi-alkali photomultiplier spectral detectors. The Multi-Area Time Lapse (MATL) acquisition feature was utilized with the 2x magnification objective lens and 1.5x digital zoom to acquire the whole tissue using transmitted light and DAPI to produce a 10% overlapped stitched image as a reference map. Transmitted light and DAPI were used to identify the tissue area and nuclear staining, respectively. Subsequently, the 40x objective lens and a 1.5x digital zoom were used to define regions of interest for acquisition on the 2x reference map. Each region created on the reference map for acquisition implemented the Z Drift Compensator (ZDC) and focus map feature. ZDC and focus map compensated for varying imaging focal points throughout the tissue with a +/- 100 μm search zone for upper and lower limits. A FITC dye channel setting was used to image CD42b for platelets and AF647 channel for CD31 blood vessels. Exposure time was set to 8.0 μs/pixel along with a 1024 x 1024 resolution and a 0.65 Airy Disk pinhole to obtain a 0.21 μm/pixel size. Although the total number of images per region of interest varies, a whole-tissue imaging experiment usually captures over 1,000 small image tiles and then montages them to create a single high-resolution digital image file, with a 10% overlap for stitching using the higher objective. Individual image tiles were saved and used for image analysis.

Automated Image Reconstruction

Deep Learning Modeling:

Each small image tile was segmented and manually labeled into four categories (benign tissue, cancer tissue, blood vessels, and background), and then one-hot-coding transformation was performed on the labeled images [1]. While the core of the convolutional neural network (CNN) model of deep learning extracted the relative position in the picture, over-cropping of the image resulted in the severe loss of the position information affecting the performance of the model [2-4]. In principle, the acquisition of more input image pixels results in more information extraction by the convolutional layer; but this requires more computational costs in CNN modeling. According to the ratio of cells and picture pixels, we choose to crop an image tile into a size of 256 x 256 x 3. The resultant dataset was divided into two parts, the training set and the testing set. The training dataset took the original image tiles (256 x 256 x 3) as input and the label image tiles (256 x 256 x 4) as the model's training target. In addition to cropping, image data were also augmented by rotation and flip [5]. With such data augmentation, we generated 4,560 original image tiles as the training dataset and 1,184 images as the testing dataset. The image datasets were randomly chosen and did not overlap [6,7].

The deep learning method, U-Net architecture, a fully convolutional neural network, was selected based on its excellent accuracy and high efficiency [8-11]. In our model, U-Net is composed of two parts, the five down sampling layers extracted the features from the input image tiles, and the up sampling structures reconstructed the segmentation image tiles. The U-Net was a symmetric structure and has the same number of layer blocks for both up and down sampling. The kernel size of the convolutional layers was identical, set as 3 x 3 [12]. The padding within a block was always 1, and the channel did not change. Instead, the padding between blocks was set as 2, and the channel doubled to ensure that down sampling blocked extract features. To avoid over-fitting, the dropout layer of a 50% ratio was added at the end layer of the last down sampling block. Symmetrically, the up sampling section started from the last layer of the deepest blocks (dropout layer) [13]. Similar to the down sampling section, the padding within a block was set as 1,

and the channel of layers stayed the same while the padding between blocks was two, and the channel was divided by 2.

Moreover, the skip connections were set between corresponding down sampling blocks and up sampling blocks to help the reconstruction [14]. However, the skip connection between the input block and the output block was canceled because of the robustness. With this structure, the output image size could be identical with the input image; therefore, the input image segmentation became the classification on every pixel (normal, cancer, vessel, and background). The batch normalization layers were set at the start of each layer except the input and the output block to help the model convergence, which was not shown in the schema. The activation function of all the convolutional layers was set as ReLU [15-17]. The last layer predicted the probability of being normal, cancer, vessel, or background for each pixel in the input image [18]. Therefore, the categorical cross-entropy was the best option for loss function because the segmentation became a four-category classification for every pixel of the input image tile [18,19].

Model Training:

All training programs were run on the cloud computing environment of Amazon web services (AWS). The models were compiled with Adam optimizer (learning rate = $1e^{-5}$) and certain cross-entropy loss function [20,21]. The batch size of each training step equaled to 8, and the epoch number equaled 50. At the end of each training step, 100 testing samples randomly chosen from the testing dataset were used as the validation to guarantee that models converge.

After accomplishing the training procedure (the categorical cross-entropy variation was less than $1e^{-4}$), the U-net model was tested on the whole test dataset. The accuracy (90.06%±0.27) and the confusion matrix (**Supplementary Figure 1a**) were calculated for every testing image. Our testing samples showed that the model indeed learned the platelet pattern. For example, 3 in **Supplementary Figure 1b**, even the manual label did not distinguish platelets

from the vessel background area due to the low contrast, but the model still could identify platelets from blood vessels. In other words, the model performed even better than labels. **Supplementary Figure 2** shows the process and the result of a full montage tissue image in the size of 30,000 x 30,000 pixels. The model segmented the original image (**Supplementary Figure 2b**) successfully, and an image of the cancerous region was generated accurately and automatically.

Platelets Quantification

To accurately detect the platelet signal distributed in the entire tissue microscopic images, platelet signal processing and detection methods were applied. **Supplementary Figure 3** shows the flowchart of our platelet quantification procedure. Platelet segmentation was the first step. In this step, the original input image (clear cancerous region image) was filtered to remove any random noise. We used an average filter of window size 3 x 3 since higher window size caused severe smoothening [22-24]. The general equation to filter an input *image, I(x,y),* using the average filter is given in equation $h[i,j] = \frac{1}{M}\sum I(x,y), x,y \in N$, where *M* is the total number of pixels in local neighborhood *N* [2,25]. The filtered image was then converted into a grayscale image. The RGB image consisted of intensity values of three color spaces or channels – Red, Green, and Blue. The platelet signals were only contained in the green channel. Therefore, RGB images were converted into grayscale images with green channel signals only. The platelet segmentation was done by histogram-based thresholding [26-28]. The histogram of the pre-processed image was generated. The x-axis in the histogram had 250 bins, and each of the bins corresponded to a gray-level value. The y-axis showed the total number of pixels corresponding to a particular bin. The number of cells presented in the input image was much higher, whereas the platelets were less in number. Some bins did not have any pixels. We eliminated all such bins because bins with zero count indicated that no pixels in the resulted image had such gray-level intensities. Also, bins

with high pixel counts ≥3,500 were eliminated since bins with such high pixel counts corresponded to cell nuclei pixels reflecting the abundancy of cell nuclei in the input image. After eliminating bins with zero and very high count, only bins containing the platelet and cell membrane pixels were acquired. Further segmentation was done by histogram-based thresholding. To set the proper threshold for binarization, we scanned all the left-over bins, and their corresponding pixel counts. The last bin represented the maximum gray level intensity that the platelets and cell membrane pixels possessed. This gray-level intensity was then used as a threshold for the segmentation of platelets and cell membrane pixels. All pixels with intensities less than the threshold were set to 1, since these pixels represented the platelet, and cell membrane pixels and others were set to 0. This process eliminated the cell nuclei leaving behind platelets and cell membranes. Then we used a cell membrane removal block to remove all cell membranes from the image. The cell membranes were eliminated by the area. Otsu's thresholding was used to remove all objects from the binary image (BW1) obtained from the previous step [29-31]. The resulted binary image (BW2) consisted of only cell membranes. To analyze only platelets and not cell membranes, we performed a binary "exclusive or" (*xor)* operation between the two binary images, BW1 and BW2, to generate the binary image consisting of only platelets after the elimination of cell membranes [32-34]. The morphological operation was the final step, where morphological operations removed the overlapping cells [35-37]. In our work, morphological opening with a disk structuring element of radius 4 (the radius was determined experimentally) has been performed on the resulting binarized image of the previous step to remove the remaining overlapping cells that appeared as thin protrusions. The output image of this phase was a binary image consisting of platelets and devoid of any other types of cells or artifacts. After platelet extraction, an automated method was built for counting the total number of platelets. The platelet segmentation process was first applied, and then the platelet count in each image was found by labeling and counting the 8-connected components or direct neighboring pixels (known as 8-connectivity) [38-41]. Platelets were of irregular shape, and also their size was quite various, so 8-connectivity was

used to count some platelets instead of 4-connectivity. The total count was summed up to find the platelet count in the image.

Transwell migration assay

We used modified Boyden chambers (8mm pore size membrane, Coster) coated with 0.1% gelatin. Fifty thousand ID8 cells and five million G-protein-deficient platelets were suspended in 100 µl serum-free media and added into the upper chamber. Platelets collected from littermates with $G^{fl/fl}$ genotypes were used as controls. Complete media containing 10% FBS (500 µl) were added to the bottom chamber as a chemoattractant in a 24-well plate. The chambers were incubated at 37°C in 5% CO2 for 6 hours. After incubation, the cells on the membrane were removed with cotton swabs. Migrating cells to the bottom of the membrane were fixed, stained, and counted by light microscopy from four random fields per membrane.

Ki67 staining

Immunostaining of resected tumor nodules for Ki67 was performed on 4-µm thick, formalin-fixed, paraffin-embedded tumor nodules. Briefly, slides were deparaffinized, antigen retrieval (pH6.0) was performed, and endogenous peroxidases and nonspecific binding were blocked. After overnight incubation with the primary Ki 67 antibody (Abcam, 1:500 dilution), slides were washed and incubated with horseradish peroxidase-conjugated secondary antibodies for 1 hour, and the slides were incubated with 100–200 µl of DAB at room temperature, counterstained with hematoxylin for 15 s, and mounted on a bright-field microscope. The number of Ki67 positive cancer cells and the total number of cancer cells in each high power field were recorded, and the percentage of Ki67 positive cells in that field was determined and reported.

Supplementary References

1. Potdar K, Pardawala TS, Pai CD. A comparative study of categorical variable encoding techniques for neural network classifiers. *International journal of computer applications*. 2017;175(4):7-9.
2. Balkwill FR, Capasso M, Hagemann T. The tumor microenvironment at a glance. *JCell Sci*. 2012;125(Pt 23):5591-5596.
3. Alom MZ, Taha TM, Yakopcic C, et al. The history began from alexnet: A comprehensive survey on deep learning approaches. *arXiv preprint arXiv:180301164*. 2018.
4. Wei Y, Xia W, Lin M, et al. HCP: A flexible CNN framework for multi-label image classification. *IEEE transactions on pattern analysis and machine intelligence*. 2015;38(9):1901-1907.
5. Shima Y. Image augmentation for object image classification based on combination of pre-trained CNN and SVM. Journal of Physics: Conference Series; 2018:012001.
6. Mikołajczyk A, Grochowski M. Data augmentation for improving deep learning in image classification problem. 2018 international interdisciplinary PhD workshop (IIPhDW): IEEE; 2018:117-122.
7. Shijie J, Ping W, Peiyi J, Siping H. Research on data augmentation for image classification based on convolution neural networks. 2017 Chinese automation congress (CAC): IEEE; 2017:4165-4170.
8. Ronneberger O, Fischer P, Brox T. U-net: Convolutional networks for biomedical image segmentation. International Conference on Medical image computing and computer-assisted intervention: Springer; 2015:234-241.
9. Ibtehaz N, Rahman MS. MultiResUNet: Rethinking the U-Net architecture for multimodal biomedical image segmentation. *Neural Networks*. 2020;121:74-87.
10. Jaeger PF, Kohl SA, Bickelhaupt S, et al. Retina U-Net: Embarrassingly simple exploitation of segmentation supervision for medical object detection. Machine Learning for Health Workshop; 2020:171-183.
11. Park J, Yun J, Kim N, et al. Fully automated lung lobe segmentation in volumetric chest CT with 3D U-net: validation with intra-and extra-datasets. *Journal of Digital Imaging*. 2020;33(1):221-230.
12. Cong J, Xiao B. Minimizing computation in convolutional neural networks. International conference on artificial neural networks: Springer; 2014:281-290.
13. Best MG, Sol N, Kooi I, et al. RNA-Seq of Tumor-Educated Platelets Enables Blood-Based Pan-Cancer, Multiclass, and Molecular Pathway Cancer Diagnostics. *Cancer Cell*. 2015;28(5):666-676.
14. Seo H, Huang C, Bassenne M, Xiao R, Xing L. Modified U-Net (mU-Net) with incorporation of object-dependent high level features for improved liver and liver-tumor segmentation in CT images. *IEEE transactions on medical imaging*. 2019;39(5):1316-1325.
15. Agarap AF. Deep learning using rectified linear units (relu). *arXiv preprint arXiv:180308375*. 2018.
16. Lomuscio A, Maganti L. An approach to reachability analysis for feed-forward relu neural networks. *arXiv preprint arXiv:170607351*. 2017.
17. Petersen P, Voigtlaender F. Optimal approximation of piecewise smooth functions using deep ReLU neural networks. *Neural Networks*. 2018;108:296-330.
18. Zhang Y-D, Pan C, Sun J, Tang C. Multiple sclerosis identification by convolutional neural network with dropout and parametric ReLU. *Journal of computational science*. 2018;28:1-10.
19. Pang T, Xu K, Dong Y, Du C, Chen N, Zhu J. Rethinking softmax cross-entropy loss for adversarial robustness. *arXiv preprint arXiv:190510626*. 2019.
20. Bock S, Goppold J, Weiß M. An improvement of the convergence proof of the ADAM-Optimizer. *arXiv preprint arXiv:180410587*. 2018.
21. Bock S, Weiß M. A proof of local convergence for the Adam optimizer. 2019 International Joint Conference on Neural Networks (IJCNN): IEEE; 2019:1-8.

22. Venkataraman S, Allison DP, Qi H, et al. Automated image analysis of atomic force microscopy images of rotavirus particles. *Ultramicroscopy*. 2006;106(8-9):829-837.
23. Boulanger J, Kervrann C, Bouthemy P, Elbau P, Sibarita JB, Salamero J. Patch-based nonlocal functional for denoising fluorescence microscopy image sequences. *IEEE Trans Med Imaging*. 2010;29(2):442-454.
24. Kushwaha HS, Tanwar S, Rathore KS, Srivastava S. De-noising Filters for TEM (Transmission Electron Microscopy) Image of Nanomaterials. 2012 Second International Conference on Advanced Computing & Communication Technologies; 2012:276-281.
25. Babashakoori S, Ezoji M. Average fiber diameter measurement in Scanning Electron Microscopy images based on Gabor filtering and Hough transform. *Measurement*. 2019;141:364-370.
26. Baradez MO, McGuckin CP, Forraz N, Pettengell R, Hoppe A. Robust and automated unimodal histogram thresholding and potential applications. *Pattern Recognition*. 2004;37(6):1131-1148.
27. Saha M, Agarwal S, Arun I, et al. Histogram Based Thresholding for Automated Nucleus Segmentation Using Breast Imprint Cytology. In: Gupta S, Bag S, Ganguly K, Sarkar I, Biswas P eds. Advancements of Medical Electronics. New Delhi: Springer India; 2015:49-57.
28. Namgung B, Ong PK, Wong YH, Lim D, Chun KJ, Kim S. A comparative study of histogram-based thresholding methods for the determination of cell-free layer width in small blood vessels. *Physiol Meas*. 2010;31(9):N61-70.
29. He T, Xue Z, Wong ST. A three-dimensional medical image segmentation app using graphic theory. 2016 IEEE-EMBS International Conference on Biomedical and Health Informatics (BHI); 2016:268-271.
30. Win KY, Choomchuay S. Automated segmentation of cell nuclei in cytology pleural fluid images using OTSU thresholding. 2017 International Conference on Digital Arts, Media and Technology (ICDAMT); 2017:14-18.
31. Osman MK, Mashor MY, Jaafar H. Performance comparison of clustering and thresholding algorithms for tuberculosis bacilli segmentation. 2012 International Conference on Computer, Information and Telecommunication Systems (CITS); 2012:1-5.
32. Umesh Adiga PS, Chaudhuri BB. Some efficient methods to correct confocal images for easy interpretation. *Micron*. 2001;32(4):363-370.
33. Jung H, Choi YS, Lee KS, et al. Logic operations based on magnetic-vortex-state networks. *ACS Nano*. 2012;6(5):3712-3717.
34. YANG Y, CAO Y, SHI W. A METHOD OF LEUKOCYTE SEGMENTATION BASED ON S COMPONENT AND B COMPONENT IMAGES. *Journal of Innovative Optical Health Sciences*. 2014;07(01):1450007.
35. Anoraganingrum D. Cell segmentation with median filter and mathematical morphology operation. Proceedings 10th International Conference on Image Analysis and Processing; 1999:1043-1046.
36. Maire E, Colombo P, Adrien J, Babout L, Biasetto L. Characterization of the morphology of cellular ceramics by 3D image processing of X-ray tomography. *Journal of the European Ceramic Society*. 2007;27(4):1973-1981.
37. He T, Xue Z, Kim Y, Wong ST. Three-dimensional dendritic spine detection based on minimal cross-sectional curvature. 2012 9th IEEE International Symposium on Biomedical Imaging (ISBI); 2012:1639-1642.
38. Ancin H, Roysam B, Dufresne TE, et al. Advances in automated 3-D image analysis of cell populations imaged by confocal microscopy. *Cytometry*. 1996;25(3):221-234.
39. Teodoro G, Kurc T, Kong J, Cooper L, Saltz J. Comparative Performance Analysis of Intel (R) Xeon Phi (TM), GPU, and CPU: A Case Study from Microscopy Image Analysis. 2014 IEEE 28th International Parallel and Distributed Processing Symposium; 2014:1063-1072.
40. Ho DJ, Salama P, Dunn K, Delp E. Boundary segmentation for fluorescence microscopy using steerable filters. Vol. 10133: SPIE; 2017.

41. Han S, Lee S, Fu C, Salama P, Dunn K, Delp E. Nuclei counting in microscopy images with three dimensional generative adversarial networks. Vol. 10949: SPIE; 2019.

Supplementary Figure 1

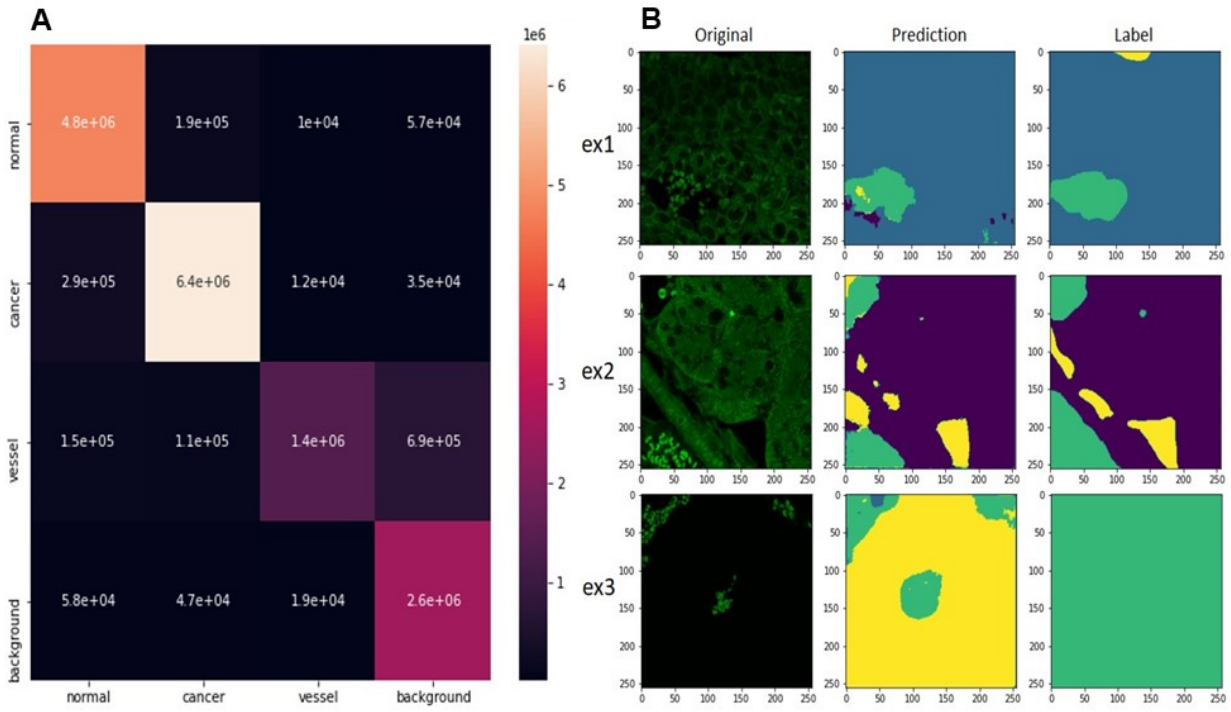

Supplementary Figure 1: ***Automated image reconstruction and modeling***. **(A)** The confusion matrix between prediction and gold standards. The x-axis represents the model predictions, and the y-axis represents the gold standard. For example, the number of the top-right block means the number of pixels classified as background while the true label is normal tissue. The overall accuracy robustly achieved 90.06% in the testing dataset despite the similarities between the platelet and background. **(B)** Three samples (256x256 pixels each) were segmented by the deep learning model, despite the similarities between platelets and background (many background-like spaces in the vessels, the model could distinguish the key platelet pattern from the original images. The predicted and labeled images include normal tissue (purple), cancer tissue (blue), platelet (green), and background (yellow).

Supplementary Figure 2

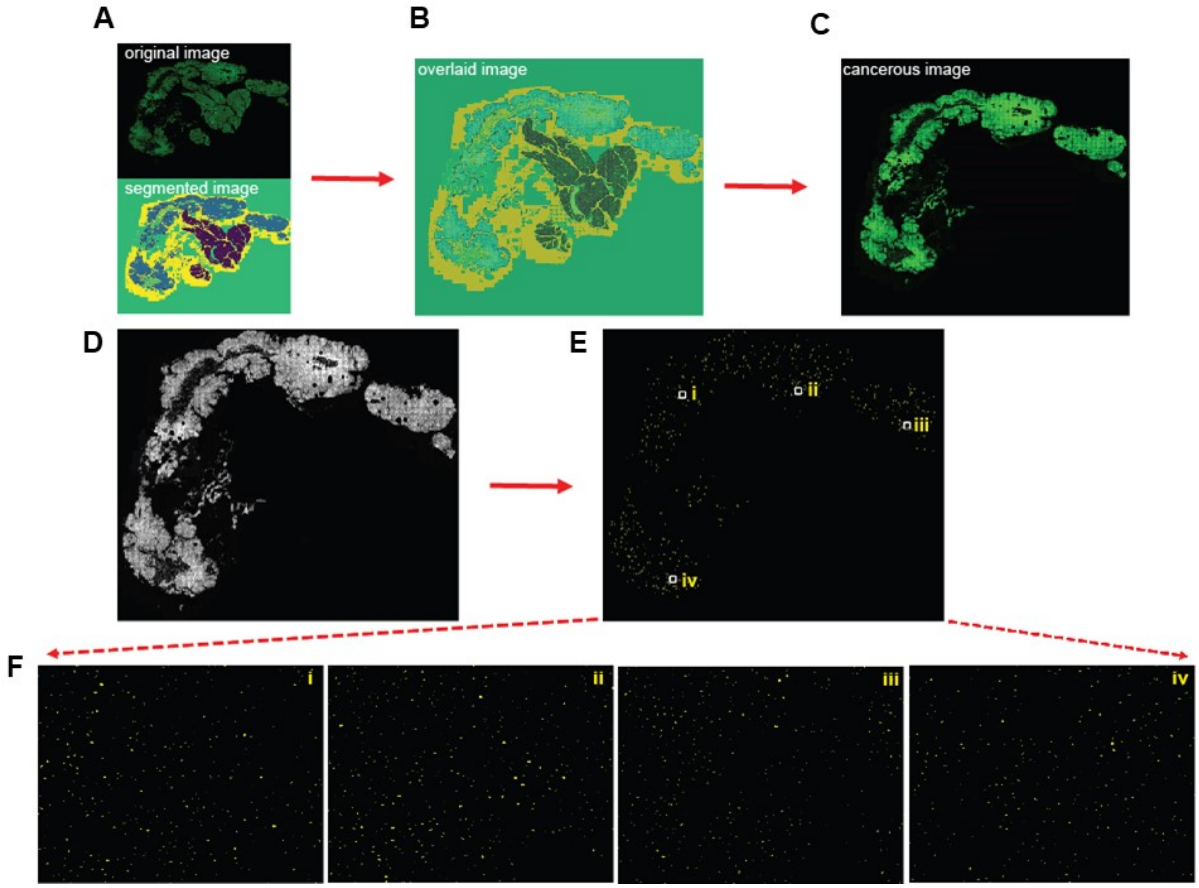

Supplementary Figure 2: ***The automatic segmentation and platelet quantification.*** During the automatic segmentation procedure, the blood vessels and the benign regions of the section were removed, and only the cancerous region was reserved, **(A)** The original images and the segmented image, respectively; **(B)** The overlapped image of the original and the segmented image; **(C)** The output image after segmentation. **D and E** show the platelets quantification procedure; **(D)** The segmented image C is translated to grayscale, the background at each edge is cut to reduce the size of the image; **E)** The binary map of the platelets after processing, and **(F)** The zoomed-in images of i, ii, iii, and iv regions in E.

Supplementary Figure 3:

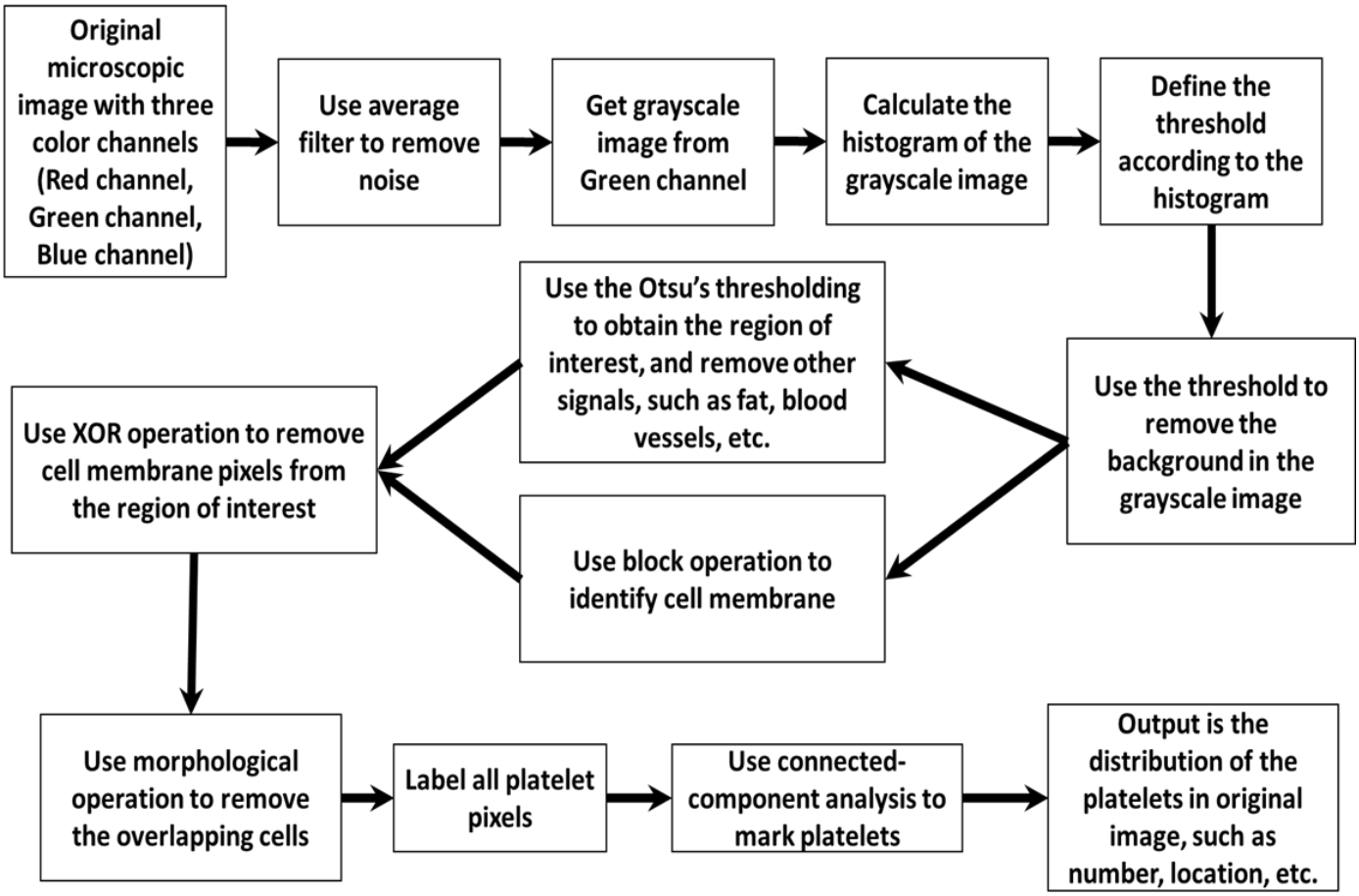

Supplementary Figure 3: ***Flowchart of platelet quantification procedure.***